Journal of Sound and Vibration (2000) **233**(4), 601–616
doi:10.1006/jsvi.1999.2842, available online at http://www.idealibrary.com on IDEAL®

FINITE ELEMENT ANALYSIS OF FLEXURAL VIBRATIONS IN HARD DISK DRIVE SPINDLE SYSTEMS

SEUNGCHUL LIM

Department of Mechanical Engineering, MyongJi University, San 38-2, *Nam-Dong, Yongin* 449-728, *South Korea*

(*Received* 22 *July* 1999, *and in final form* 2 *December* 1999)

This paper is concerned with the flexural vibration analysis of the hard disk drive (HDD) spindle system by means of the finite element method. In contrast to previous research, every system component is here analytically modelled taking into account its structural flexibility and also the centrifugal effect particularly on the disk. To prove the effectiveness and accuracy of the formulated models, commercial HDD systems with two and three identical disks are selected as examples. Then their major natural modes are computed with only a small number of element meshes as the shaft rotational speed is varied, and subsequently compared with the existing numerical results obtained using other methods and newly acquired experimental ones. Based on such a series of studies, the proposed method can be concluded as a very promising tool for the design of HDDs and various other high-performance computer disk drives such as floppy disk drives, CD ROM drives, and their variations having spindle mechanisms similar to those of HDDs.

1. INTRODUCTION

The hard disk drive (HDD) is the most popular and has the largest capacity of all kinds of contemporary, auxiliary memory devices for personal computers. Nowadays, its spindle system consists of a spindle shaft (or a hub), stacked disks of the same dimension, and two ball bearings as illustrated in Figure 1. It is obvious that as the number of hard disks increases, so does the HDD data storage capacity. However, from the viewpoint of cost, it is known to be more economical to maximize the data density of each disk rather than the total number of multiple disks. Thus, each disk is lately being required to store more than two Giga bytes of digital data, which in turn means that the vibrational magnitude of the uncontrollable, non-repeatable runout on a track should be limited to within 0·1 μm to prevent the so-called misregistration of the magnetic heads during the track-following servo process. Besides, for fast data access, the disks in some HDDs tend to rotate at as high a speed as 10 000 rpm.

Such a circumstance requires that for precision analysis the hard disks not be treated as rigid any longer, and more appropriate tools for HDD spindle vibration analysis are in need than ever before. As the desired feature of such tools, the capability of analyzing coupled as well as uncoupled vibration modes can be specified above all.

However, previous research work in the area of rotor vibrations was mostly done by assuming either the shaft or the disk to be rigid [1–4]. Meanwhile, some other work was carried out by relaxing such assumption so as to reveal the elastic, coupled vibrations between the shaft and the disks [5–7]. But, even such work made use of the simple Rayleigh–Ritz method [8]. In those respects, both approaches inevitably suffer from

0022-460X/00/240601 + 16 $35.00/0

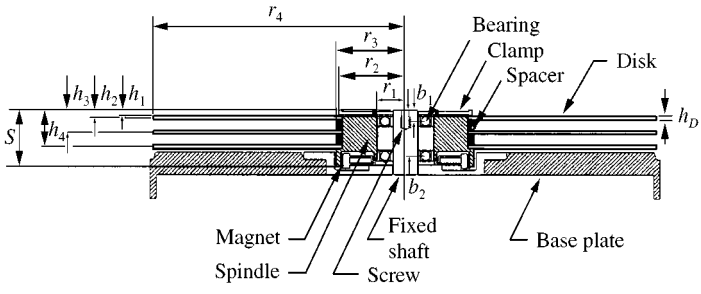

Figure 1. Hard disk drive spindle system.

computational inaccuracy and the limited capability of analyzing higher, coupled vibrational modes. This becomes more serious particularly in the case of actual HDD spindle systems with hubs made of rather complex shapes and many different materials.

Hence, in this work every system component is analytically modelled taking into account its structural flexibility and also the centrifugal effect particularly on the disk. In the sequel, such finite element models are assembled and applied to the commercial HDDs as examples to prove the effectiveness and accuracy of the proposed approached based on the experimental results. On the other hand, since the most critical factor on which the aforementioned storage density enhancement depends is the transverse, flexural vibrations of the spindle, they are the only matter of interest here as far as the spindle is concerned.

2. ELEMENT EQUATIONS OF MOTION

In this paper, the equations of motion for each element are derived with due considerations of the centrifugal and Coriolis forces caused by the rotational motion. To this end, throughout the procedure it is assumed that the system is isotropic, and the associated deflections are all elastic and small enough.

To describe an orientation in the 3-D space, a set of Euler angles involved in the successive rotations about the X-, Y-, and Z-axis are defined to be $(\Omega t, \theta_\xi, \theta_\eta)$ with the following co-ordinate frames used:

$OX_0Y_0Z_0$—fixed inertial co-ordinate frame: $\{0\}$,
$OX_1Y_1Z_1$—co-ordinate frame rotating about X_0-axis at a constant speed Ω with respect to $\{0\}:\{1\}$,
$OX_2Y_2Z_2$—co-ordinate frame rotating θ_η about the Z-axis of the intermediate frame which rotates θ_ξ about the Y_1-axis with respect to $\{1\}:\{2\}$.

Among those, frame $\{2\}$ corresponds to the shaft-fixed frame undergoing the shaft's elastic rotations as well. Since all the elastic deflections of the shaft and the disks are to be expressed, respectively, in the rotating frames $\{1\}$ and $\{2\}$, the resulting equations of motion will be relatively simple and time-invariant without the appearance of the rotation angle Ωt, which is the product of the rotational speed and the lapse time t.

In such a case, the absolute angular velocity of a body in space can be graphically obtained. Retaining its terms only up to the second order,

$$^2(^0\omega_2) = [\Omega\{1 - (\theta_\eta^2 + \theta_\xi^2)/2\} + \theta_\eta\dot{\theta}_\xi, \dot{\theta}_\xi - \Omega\theta_\eta, \dot{\theta}_\eta + \Omega\theta_\xi]^{\mathrm{T}}, \tag{1}$$

where the leading superscript outside the parentheses denotes the frame, along whose axes the corresponding vector is expressed componentwise, while the other superscript inside represents the reference frame where the vector quantity of the body or the frame denoted by the trailing subscript is observed. Henceforth, if the two superscripts are the same, both the parentheses and one of those will be omitted.

On the other hand, when c and s abbreviate, respectively, the cosine and sine functions, the rotation matrix between the defined co-ordinate frames are as follows:

$$ {}^1R_0 = \begin{bmatrix} 1 & 0 & 0 \\ 0 & c(\Omega t) & s(\Omega t) \\ 0 & -s(\Omega t) & c(\Omega t) \end{bmatrix}, \quad {}^2R_1 = \begin{bmatrix} 1 & \theta_\eta & -\theta_\xi \\ -\theta_\eta & 1 & 0 \\ \theta_\xi & 0 & 1 \end{bmatrix}. \tag{2a, b} $$

Whenever necessary, other rotation matrices can be readily obtained using its concatenation arithmetics or the orthonormality property.

2.1. SHAFT (HUBS, SPACERS, AND CLAMPS)

Whether hollow or now, a shaft representing the hub, the spacer, or the clamp is subdivided into several finite elements to be modelled, one of which is shown in Figure 2. Until now, there have existed various beam models for transverse, bending kinematics. Among them, taking into account the rotary inertia arising necessarily from the thick and short shape of the shaft at hand, the Rayleigh's beam theory is to be adopted.

In that case, the position vector of the typical point S on a cross-section in Figure 2 is

$$ \underline{w}_S = \underline{x}_S + \underline{u}_S + \underline{r}_S, \tag{3a} $$

from the origin O after the deflection takes place. If the above equation is rewritten componentwise in a matrix form,

$$ {}^0\mathbf{w}_S = {}^0R_1({}^1\mathbf{x}_s + {}^1\mathbf{u}_s) + {}^0R_2{}^2\mathbf{r}_S, \tag{3b} $$

where ${}^1\mathbf{x}_D = [x\ 0\ 0]^{\mathrm{T}}$ denotes the nominal position vector of the point S along the shaft, ${}^1\mathbf{u}_s = [0\ v(x,t)\ w(x,t)]^{\mathrm{T}}$ the lateral deflection vector of the shaft centerline, and

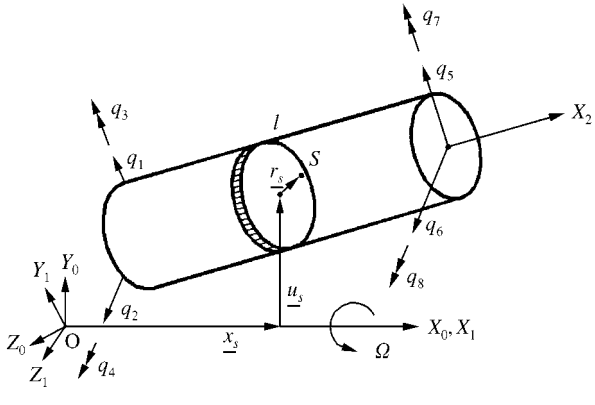

Figure 2. Finite shaft element.

${}^2\mathbf{r}_s = [0\ rc\theta\ rs\theta]^{\mathrm{T}}$ the nominal position vector of the point S on the cross-section, r and θ being, respectively, the radial and circumferential co-ordinates.

Time differentiation of equation (3b) in frame $\{0\}$ leads to the absolute velocity vector

$$ {}^0\dot{\mathbf{w}}_S = {}^0\tilde{\omega}_1\ {}^0R_1({}^1\mathbf{x}_S + {}^1\mathbf{u}_s) + {}^0R_1\,{}^1\dot{\mathbf{u}}_S + {}^0\tilde{\omega}_2\,{}^0R_2\,{}^2\mathbf{r}_s, \tag{4} $$

where " $\sim$ " stands for the 3×3 skew-symmetric matrix made up of the corresponding vector elements to replace the vector cross product. It is noteworthy that the last term in the above equation relates to the rotary inertia effect from the beam cross-section, and could be ignored if the classical beam theory were applied.

On the other hand, discretizing the distributed variables in space according to the assumed modes method [8] results in equations of motion in a desirable form, i.e., ordinary differential equations. Hence, when the flexural, elastic deflections are assumed as

$$ v(x,t) = \boldsymbol{\varphi}_S^{\mathrm{T}}(x)\mathbf{q}_y(t), \quad w(x,t) = \boldsymbol{\varphi}_s^{\mathrm{T}}(x)\mathbf{q}_z(t), \tag{5a, b} $$

the following also hold true according to the beam kinematics:

$$ \theta_\xi(x,t) = -\,\boldsymbol{\phi}_S^{\mathrm{T}}(x)\mathbf{q}_z(t), \quad \theta_\eta(x,t) = \boldsymbol{\phi}_S^{\mathrm{T}}(x)\mathbf{q}_y(t), \tag{5c, d} $$

in which $\boldsymbol{\phi}_S(x) = \partial\boldsymbol{\varphi}_S(x)/\partial x$.

In consideration of equations (4) and (5), the kinetic energy can be obtained as

$$ T_s^e = \frac{\Omega^2}{2}\left\{\int_x I_{Sp}\,\mathrm{d}x + \mathbf{q}_y^{\mathrm{T}}G_S^e\mathbf{q}_y + \mathbf{q}_z^{\mathrm{T}}G_S^e\mathbf{q}_z\right\} + \Omega\{\mathbf{q}_y^{\mathrm{T}}G_S^e\dot{\mathbf{q}}_z - \mathbf{q}_z^{\mathrm{T}}M_S^e\dot{\mathbf{q}}_y\} + \frac{1}{2}\{\dot{\mathbf{q}}_y^{\mathrm{T}}M_S^e\dot{\mathbf{q}}_y + \dot{\mathbf{q}}_z^{\mathrm{T}}M_S^e\dot{\mathbf{q}}_z\}, \tag{6} $$

where $G_S^e = \int_x(\rho_S A_S\boldsymbol{\varphi}_S\boldsymbol{\varphi}_S^{\mathrm{T}} - I_{Sp}\boldsymbol{\phi}_S\boldsymbol{\phi}_S^{\mathrm{T}}/2)\,\mathrm{d}x$, $M_S^e = \int_x(\rho_S A_S\boldsymbol{\varphi}_S\boldsymbol{\varphi}_S^{\mathrm{T}} + I_{Sp}\boldsymbol{\phi}_S\boldsymbol{\phi}_S^{\mathrm{T}}/2)\,\mathrm{d}x$, and ρ_S, A_S, and I_{Sp} designate, respectively, the mass density, the cross-sectional area, and the polar mass moment of inertia per unit length. Meanwhile, the potential energy is stored in the shaft when it is bent. Hence, if the bending rigidity of the shaft is $E_S I_S$, and the stiffness matrix $K_S^e = \int_x E_S I_S\boldsymbol{\varphi}_S''\boldsymbol{\varphi}_S''^{\mathrm{T}}\,\mathrm{d}x$, then the potential energy will amount to

$$ V_S^e = \tfrac{1}{2}(\mathbf{q}_y^{\mathrm{T}}K_S^e\mathbf{q}_y + \mathbf{q}_z^{\mathrm{T}}K_S^e\mathbf{q}_z). \tag{7} $$

In addition, when ${}^2f = [0\ f_y\ f_z]^{\mathrm{T}}$ denotes the external force including the centrifugal force originating from the unbalance mass, the non-conservative virtual work is expressed as

$$ \delta\bar{W}_S = \int_D f_y\boldsymbol{\varphi}_S^{\mathrm{T}}\,\mathrm{d}D\ \delta\mathbf{q}_y + \int_D f_z\,\boldsymbol{\varphi}_S^{\mathrm{T}}\,\mathrm{d}D\ \delta\mathbf{q}_z. \tag{8} $$

When put into the Lagrange equation [8], the energies in equations (6)–(8) yield the equations of motion for the shaft element as follows:

$$ \begin{bmatrix} M_S^e & 0 \\ 0 & M_S^e \end{bmatrix}\begin{Bmatrix}\ddot{\mathbf{q}}_y \\ \ddot{\mathbf{q}}_z\end{Bmatrix} + \Omega\begin{bmatrix} 0 & -(M_S^e + G_S^e) \\ (M_S^e + G_S^e) & 0 \end{bmatrix}\begin{Bmatrix}\dot{\mathbf{q}}_y \\ \dot{\mathbf{q}}_z\end{Bmatrix} $$
$$ + \begin{bmatrix} (K_S^e - \Omega^2 G_S^e) & 0 \\ 0 & (K_S^e - \Omega^2 G_S^e) \end{bmatrix}\begin{Bmatrix}\mathbf{q}_y \\ \mathbf{q}_z\end{Bmatrix} = \int_D \begin{Bmatrix} f_y \\ f_z\end{Bmatrix}\boldsymbol{\varphi}_S\,\mathrm{d}D. \tag{9a} $$

In the preceding equation, if the real generalized co-ordinates and force vectors are substituted with the complex ones such that $\mathbf{z}_S = \mathbf{q}_y + \mathrm{j}\mathbf{q}_z$ and $Q_S = f_y + \mathrm{j}f_z$, the number of

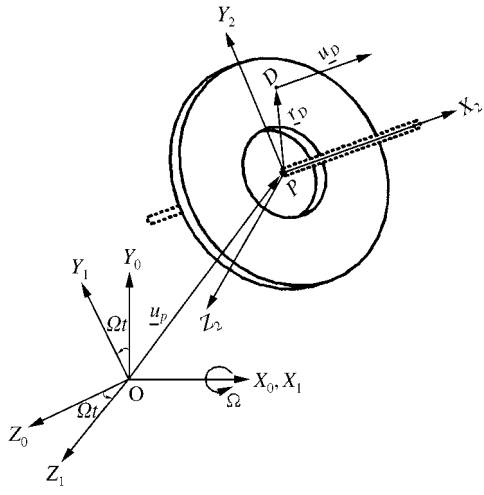

Figure 3. Annular disk element.

constituent scalar equations can be halved so that

$$M_S^e \ddot{\mathbf{z}}_S + \mathrm{j}\Omega(M_S^e + G_S^e)\dot{\mathbf{z}}_S + (\mathbf{K}_S^e - \Omega^2 G_S^e)\mathbf{z}_S = \int_D Q_S \boldsymbol{\varphi}_S \, \mathrm{d}D, \tag{9b}$$

where $\mathrm{j} = \sqrt{-1}$.

Consequently, the finite shaft element has two complex degrees of freedom at each end as depicted in Figure 2.

2.2. DISK (HARD DISKS)

It is known that the flexural spindle vibration may cause fatal errors during the data read/write process in HDDs, and only the out-of-plane vibration of the disk is coupled with it. Therefore, in this paper, the vibration of the disk in the direction perpendicular to the disk plane is to be exclusively investigated. Although the hard disk itself has the shape of an annulus, it is subdivided into concentric annular disk elements for precision analysis.

One of them is typically illustrated in Figure 3, where the displacement vector from the origin O on the element is

$${}^0\mathbf{w}_D = {}^0R_1 \, {}^1\mathbf{u}_P + {}^0R_2({}^2\mathbf{r}_D + {}^2\mathbf{u}_D) \tag{10}$$

in a deformed state. In the above equation, ${}^1\mathbf{u}_P = [x_D \;\; v_D \;\; w_D]^{\mathrm{T}}$ represents the position vector of the element center located at x_D along the shaft, ${}^2\mathbf{r}_D = [0 \;\; rc\theta \;\; rs\theta]^{\mathrm{T}}$ the nominal position vector of the point D on the disk element, and ${}^2\mathbf{u}_D = [u_D(r, \theta, t) \;\; 0 \;\; 0]^{\mathrm{T}}$ the elastic disk deflection out of the element plane.

As in equation (5), the distributed variable $u_D(r, \theta, t)$ needs to be variable separated. In doing so, note that it is a periodic function with a period of 2π in the circumferential direction. Hence, it can be expanded into a Fourier infinite series in that direction. However, since only the disk modes with one nodal diameter are related to the coupled vibrations [5], the fundamental harmonic terms should be all terms not to be truncated in the series to analyze those vibrations. In such a context, introducing the function of radial position $\boldsymbol{\varphi}_D$

and the time-dependent generalized co-ordinates $\mathbf{q}_{Dc}$ and $\mathbf{q}_{Ds}$ as coefficients, $\mathbf{u}_D$ can be separated into

$$\mathbf{u}_D(r,\theta,t) = \boldsymbol{\varphi}_D^{\mathrm{T}}(r)\, cn\theta\, \mathbf{q}_{Dc}(t) + \boldsymbol{\varphi}_D^{\mathrm{T}}(r)\, sn\theta\, \mathbf{q}_{Ds}(t), \quad n = 1. \tag{11}$$

Inserting into the following formula the time derivative of equation (10) combined with equation (11), one can get the kinetic energy expression for the annular disk element, which is detailed in Appendix A:

$$T_D^e = \frac{1}{2}\int_m {}^0\dot{\mathbf{w}}_D^{\mathrm{T}}\, {}^0\dot{\mathbf{w}}_D \,\mathrm{d}m. \tag{12}$$

There, $\Psi_S(x_D) = \boldsymbol{\varphi}_S(x_D)\boldsymbol{\varphi}_S^{\mathrm{T}}(x_D)$, $\Phi_S(x_D) = \boldsymbol{\phi}_S(x_D)\boldsymbol{\phi}_S^{\mathrm{T}}(x_D)$, and $\Phi_{SD}(x_D) = \boldsymbol{\phi}_S(x_D)\bar{\boldsymbol{\varphi}}_D^{\mathrm{T}}(x_D)$. Also, if m_D^e, I_{Dy}, I_{Dp}, ρ_D, h_D, R_i and R_0, respectively, denote the element mass, the diametral and the polar mass moments of inertia, the mass density, the element thickness, the inner and outer radii, then $\bar{\boldsymbol{\varphi}}_D = \int_{R_i}^{R_0} \pi\rho_D h_D r^2 \boldsymbol{\varphi}_D \,\mathrm{d}r$ and $M_D^e = \int_{R_i}^{R_0} \pi\rho_D h_D \boldsymbol{\varphi}_D \boldsymbol{\varphi}_D^{\mathrm{T}} r \,\mathrm{d}r$. For reference, $I_{Dp} = 2I_{Dy}$ in the case of thin circular plates.

On the other hand, the potential energy for the disk element stems not only from the bending deformation but also the initial stress strain, which is in the present case associated with the centrifugal force due to rotation. Accordingly,

$$V_D^e = \tfrac{1}{2}\{\mathbf{q}_{Dc}^{\mathrm{T}}(K_{De} + K_{Dg})\mathbf{q}_{Dc} + \mathbf{q}_{Ds}^{\mathrm{T}}(K_{De} + K_{Dg})\mathbf{q}_{Ds}\} \tag{13}$$

in which K_{De} denotes the generic stiffness matrix depending on the plate's bending rigidity D_E and the Poisson ratio ν as in Appendix B, E_D being the Young's modulus. Moreover, K_{Dg} is called the geometric stiffness matrix taking the form in Appendix B due to the initial stress strain, where σ_r and σ_θ mean the normal stress components in the disk element, respectively, in the radial and circumferential directions. Provided the disk is thin enough and the stresses are axisymmetrically distributed, the shear stress components in the plane can be neglected such that $\tau_{r\theta} = \tau_{\theta r} = 0$ and the aforementioned normal stresses are obtained as proportional to Ω^2 [5, 9]. Therefore, if the rotational speed goes far beyond the regular operating range, the geometric stiffness will become more and more dominant so that the disk may behave as a rigid body.

Just as in the shaft element, the distributed forces in the disk element plane including the centrifugal forces may cause the non-conservative virtual work

$$\delta\bar{W}_D = \int_D f_y \,\mathrm{d}D\, \boldsymbol{\varphi}_S^{\mathrm{T}}(x_D)\, \delta\mathbf{q}_y + \int_D f_z \,\mathrm{d}D\, \boldsymbol{\varphi}_S^{\mathrm{T}}(x_D)\, \delta\mathbf{q}_z, \tag{14}$$

where a distinction lies in that $\boldsymbol{\varphi}_S(x_D)$ above is the shaft shape function evaluated at the disk-mounted position.

When equations (12)–(14) are put into the Lagrange equation with a complex generalized co-ordinate and a force introduced as $\mathbf{z}_D = \mathbf{q}_{Dc} + \mathrm{j}\mathbf{q}_{Ds}$ and $Q_D = f_y + \mathrm{j}f_z$, the equations of motion for the disk element are derived as

$$\begin{bmatrix} m_D^e\Psi_D(x_D) + I_{Dy}\Phi_S(x_D) & -\Phi_{SD}(x_D) \\ -\Phi_{SD}(x_D) & M_D^e \end{bmatrix} \begin{Bmatrix} \ddot{\mathbf{z}}_S \\ \ddot{\mathbf{z}}_D \end{Bmatrix} + \mathrm{j}\Omega \begin{bmatrix} 2m_D^e\Psi_D(x_D) + (I_{Dp} - 2I_{Dy})\Phi_S(x_D) & 0 \\ 0 & 0 \end{bmatrix} \begin{Bmatrix} \dot{\mathbf{z}}_S \\ \dot{\mathbf{z}}_D \end{Bmatrix}$$
$$+ \begin{bmatrix} -\Omega^2\{m_D^e\Psi_S(x_D) + (I_{Dy} - I_{Dp})\Phi_S(x_D)\} & -\Omega^2\Phi_{SD}(x_D) \\ -\Omega^2\Phi_{SD}^{\mathrm{T}}(x_D) & K_{De} + K_{Dg} \end{bmatrix} \begin{Bmatrix} \mathbf{z}_S \\ \mathbf{z}_D \end{Bmatrix} = \begin{Bmatrix} \boldsymbol{\varphi}_S(x_D)\int_D Q_D \,\mathrm{d}D \\ \mathbf{0} \end{Bmatrix}. \tag{15}$$

2.3. BEARING

The bearings in HDD are of the deep groove type so as to support the spindle both in the radial and longitudinal directions. For the present purpose, however, they are merely modelled to oppose its transverse motion as a massless spring and damper. Under such an assumption, the kinetic energy vanishes, and the potential energy equals the negated work done by the spring force, i.e.,

$$V_B = -\int {}^1\mathbf{f}_c^{\mathrm{T}}\, \mathrm{d}\,{}^1\mathbf{u}_B, \tag{16a}$$

where ${}^1\mathbf{f}_c = -k_B\,{}^1\mathbf{u}_B$ and ${}^1\mathbf{u}_B = [0\ \ v_B\ \ w_B]^{\mathrm{T}}$, respectively, refer to the spring force and the elastic shaft displacement at the bearing location x_B along the shaft, and k_B the stiffness coefficient for the isotropic bearings. Going through some algebra, one can rearrange the above equation as

$$V_B = \frac{k_B}{2}\{\mathbf{q}_y^{\mathrm{T}}\boldsymbol{\varphi}_S(x_B)\boldsymbol{\varphi}_S^{\mathrm{T}}(x_B)\mathbf{q}_y + \mathbf{q}_z^{\mathrm{T}}\boldsymbol{\varphi}_S(x_B)\boldsymbol{\varphi}_S^{\mathrm{T}}(x_B)\mathbf{q}_z\}. \tag{16b}$$

On the other hand, the total non-conservative force including the damping force, say ${}^1\mathbf{f}_{nc}$, contributes to the virtual work

$$\delta\bar{W}_B = {}^1\mathbf{f}_{nc}^{\mathrm{T}}\delta\,{}^1\mathbf{u}_B. \tag{17a}$$

When the element damping matrix $C = diag\,[0, c_B, c_B]$, and the external bearing force ${}^1\mathbf{Q} = [0, f_{By}, f_{Bz}]^{\mathrm{T}}$, it holds that ${}^1\mathbf{f}_{nc} = -C\,{}^1\mathbf{R}_0\,{}^0\dot{\mathbf{u}}_B + {}^1\mathbf{Q}$. As a result, the above equation concerning the virtual work leads to

$$\begin{aligned}\delta\bar{W}_B = &\{f_{By} - c_B(\boldsymbol{\varphi}_S^{\mathrm{T}}(x_B)\dot{\mathbf{q}}_y - \Omega\boldsymbol{\varphi}_S^{\mathrm{T}}(x_B)\mathbf{q}_z)\}\,\boldsymbol{\varphi}_S^{\mathrm{T}}(x_B)\,\delta\mathbf{q}_y\\ &+\{f_{Bz} - c_B(\boldsymbol{\varphi}_S^{\mathrm{T}}(x_B)\dot{\mathbf{q}}_z + \Omega\boldsymbol{\varphi}_S^{\mathrm{T}}(x_B)\mathbf{q}_y)\}\,\boldsymbol{\varphi}_S^{\mathrm{T}}(x_B)\delta\mathbf{q}_z.\end{aligned} \tag{17b}$$

By inserting equations (16b) and (17b) into the Lagrange equation, the equations of motion for the bearing element can be obtained as

$$c_B\Psi_S(x_B)\dot{\mathbf{z}}_S + (\mathbf{k}_B + \mathrm{j}c_B\Omega)\Psi_S(x_B)\mathbf{z}_S = \boldsymbol{\varphi}_S(x_B)Q_B, \tag{18}$$

where $\Psi_S(x_B) = \boldsymbol{\varphi}_S(x_B)\boldsymbol{\varphi}_S^{\mathrm{T}}(x_B)$, and $Q_B = f_{By} + \mathrm{j}f_{Bz}$. On the other hand, if equation (18) is used as it is, the bearing element will have as many as four complex degrees of freedom (d.o.f.s) like the shaft element does. However, in consideration of its actual motions occurring only in the translational manner at a specific node, it is clear that there remains a necessity to further refine equation (18).

3. SPATIAL DISCRETIZATION AND SHAPE FUNCTIONS

Since all the elements treated in this paper experience only the bending deformation, they belong to the fourth order eigenvalue problem. Hence, a set of the Hermite cubic polynomials [10] is appropriate as the shape functions for the spatial discretization.

In other words, for the shaft element one can use $\boldsymbol{\varphi}_S(x) = [\varphi_{S1}(x)\ \ \varphi_{S2}(x)\ \ \varphi_{S3}(x)\ \ \varphi_{S4}(x)]^{\mathrm{T}}$, where $\boldsymbol{\varphi}_{S_i}$ $(i = 1, 2, 3, 4)$ represents the following function of the

non-dimensionalized local co-ordinate $\xi = x/l$;

$$\varphi_{S1}(\xi) = 1 - 3\xi^2 + 2\xi^3, \quad \varphi_{S2}(\xi) = l\xi(\xi - 1)^2, \quad \varphi_{S3}(\xi) = 3\xi^2 - 2\xi^3, \quad \varphi_{S4}(\xi) = l\xi^2(\xi - 1). \tag{19}$$

Therefore, when the generalized co-ordinates are defined to be $\mathbf{q}_y(t) = [q_1 \ q_4 \ q_5 \ q_8]^T$ and $\mathbf{q}_z(t) = [q_2 \ q_3 \ q_6 \ q_7]^T$ in terms of the nodal displacements in Figure 2, certain physical relationships hold for the elastic displacements at the boundary:

$$q_1 = v(0, t), \quad q_2 = w(0, t), \quad q_3 = w'(0, t), \quad q_4 = v'(0, t),$$

$$q_5 = v(l, t), \quad q_6 = w(l, t), \quad q_7 = w'(l, t), \quad q_8 = v'(l, t).$$

Likewise, for equation (11) regarding the disk element, the admissible functions and the generalized co-ordinates are defined, respectively, as $\boldsymbol{\varphi}_D(r) = [\varphi_{D1} \ \varphi_{D2} \ \varphi_{D3} \ \varphi_{D4}]^T$ and $\mathbf{q}_{Di}(t) = [q_{Di1} \ q_{Di2} \ q_{Di3} \ q_{Di4}]^T$, where $i = c$ or s. However, $\boldsymbol{\varphi}_D$ differs from $\boldsymbol{\varphi}_S$ in that its local independent variable is $\xi = (r - R_i)/(R_0 - R_i)$, and the element width $(R_0 - R_i)$ takes the place of the shaft element length l. With such shape functions applied, each coefficient matrix in the element equations of motion can be constructed in a closed form. But, for the sake of brevity, further details are to be omitted.

Up to this point, in terms of the total number of complex d.o.f.'s, the shaft element has four, the disk element eight, and lastly the bearing element four of them. However, except for the shaft element, there exists undesirable redundancy.

As for the disk element, to describe its actual motion a total of three nodes will suffice provided that the first of those is situated at the disk center coincident with the specific shaft node, the second at the inner circumference, and the third at the outer circumference. Hence, allocating two complex d.o.f.'s to each node adds up to only six d.o.f.'s in total. Discarding extra null elements in consideration of equation (19) at the first nodal points leads to $\boldsymbol{\varphi}_S(x_D) = [1 \ 0]^T$ and $\boldsymbol{\varphi}_S(x_D) = [0 \ 1]^T$ relevant to equation (15). These in turn reduce the size of all the coefficient matrices down to 6×6, and also that of the generalized co-ordinate to 6×1. In the disk element assemblage procedure, care should be taken regarding the aspect that for the innermost disk element, no d.o.f.'s exist at the second node due to the clamped boundary condition with the shaft. This sort of disk element is referred to as the shaft-disk transition element in reference [4].

On the other hand, equation (18) for the bearing element has the same kind of problem as addressed beforehand. Since only a single complex d.o.f. is required in actuality to describe the bearing's translational motion, the extra ones must be eliminated. If the bearing location x_B coincides with a shaft node, it will turn out that $\boldsymbol{\varphi}_S(x_B) = 1$ discarding the other three null elements. In such a case, if either the first or the third element of $\mathbf{z}_S$ vector in equation (18) is only chosen to be renamed as z_B, equation (18) can be simplified as a scalar equation:

$$c_B\dot{z}_B + (k_B + \mathrm{j}c_B\Omega)z_B = Q_B. \tag{20}$$

4. COMPUTATIONAL AND EXPERIMENTAL RESULTS

Those developed finite element models are all computer programmed. Hence, given any particular rotor system configuration, overall equations of motion can be promptly assembled using the connectivity matrix method [10], and recast into a state-space form from which the standard eigenvalue problem is to be solved.

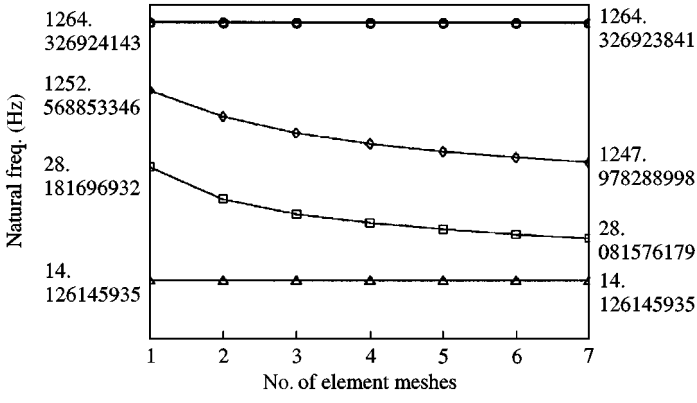

Figure 4. Natural frequencies versus the no. of disk meshes.

4.1. CONVERGENCE CHARACTERISTICS

Before being applied to real problems, the formulated finite element models are evaluated *a priori* in terms of the convergence characteristics. To this end, the coupled lowest four modes are investigated for a uniform rotor model which carries a thin disk at the midpoint of a slender shaft. The shaft is assumed to be simply supported at both extreme ends. Then, each system component is subdivided in order for the element meshes to have equal lengths or widths.

First, with the total number of shaft element meshes fixed as six, disk element meshes are increased from one to six. In such a case, as can be seen in Figure 4, the second and the third modes are relatively more sensitive to the number of disk meshes than the other modes until they almost converge. This phenomenon is closely tied with the mode shapes since the disk deforms considerably not in the first and fourth modes but in the other two modes. Next, conversely the number of shaft meshes is multiplied while that of disk meshes continues to equal six. In this case, Figure 5 shows that due to the same reason, the third and fourth modes are more sensitive but rapidly converge as the shaft meshes increases.

Based on the above observations, it can be justified to use five and two element meshes, respectively, for a hard disk and a uniform section of the spindle shaft.

4.2. NATURAL MODES

In order to demonstrate the accuracy of the proposed models, the commercial HDD spindle system with duplicate disks in reference [5] is taken as the first example although it was originally idealized to some extent. With exactly the same data input for the sizes and the material constants, its natural modal characteristics are computed employing only five element meshes equally for both the whole spindle shaft and each disk for enough convergency, while the shaft rotational speed is varied. All the major flexural modes are investigated including the uncoupled disk modes, and compared with the existing, plotted results obtained using the Rayleigh–Ritz method in conjunction with as many as 40 admissible functions in total [5].

In Figure 6, the natural frequencies up to the six-coupled mode are presented in the inertial frame $\{0\}$, and also in Figure 7 the corresponding mode shapes in non-rotating state are exhibited. Note here that all the Campbell diagrams in this paper are plotted with

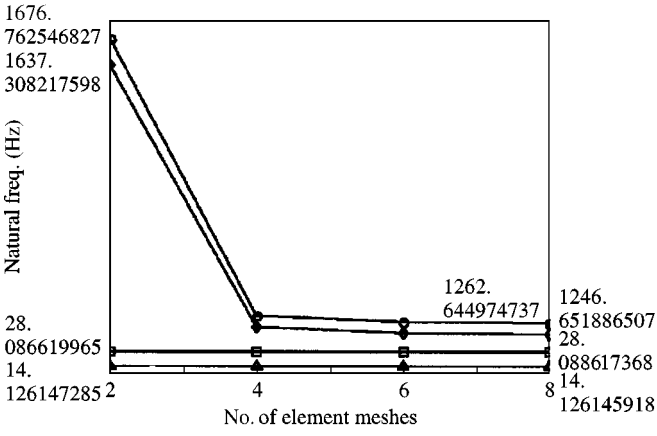

Figure 5. Natural frequencies versus the no. of shaft meshes.

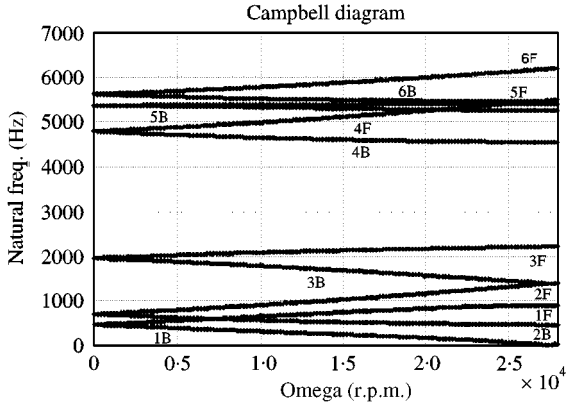

Figure 6. Coupled modes (2 disks).

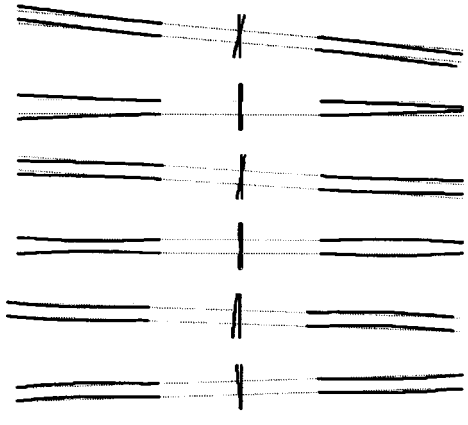

Figure 7. Mode shapes (2 disks): from the top, first to sixth mode.

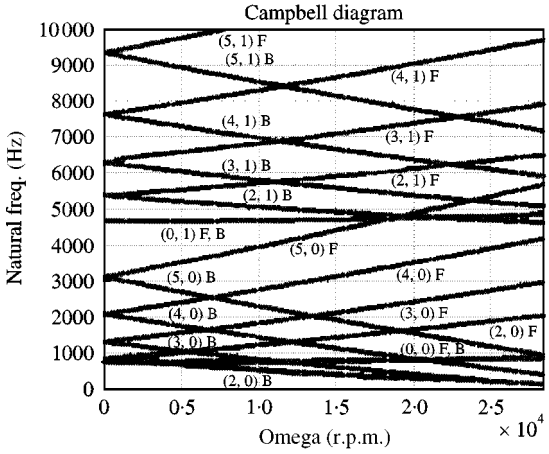

Figure 8. Uncoupled disk modes (2 disks).

respect to that frame for comparison purposes with the experimental results. They are in good agreement with the existing results up to the fourth mode whether or not the whirl directions are forward (F) or backward (B). However, in the fifth mode, a simultaneous rocking motion of the shaft is more evidently discovered besides the translational vibration to the side. Also, the sixth mode is additionally sought similar to the third mode except for another nodal circle. According to the terms in reference [3], such modes as the second and fourth modes can be classified as the balanced modes as opposed to the other four unbalanced modes.

On the other hand, letting $n \neq 1$ unlike in equation (11) is equivalent to considering the constant or the higher harmonic terms in the Fourier series expansion. It enables the uncoupled disk vibration modes to be computed as in Figure 8, where the first and the second numerals in the parentheses indicate, respectively, the number of nodal diameters and nodal circles each mode shape possesses. As far as all the lower modes of less than five diametral and two circular nodes in reference [5] are concerned, the values look very close.

As a second example, the trendier HDD system is selected with three identical disks mounted on a rather complex-shaped spindle as in Figure 1, where $r_1 = 6{\cdot}5$ mm, $r_2 = 15{\cdot}0$ mm, $r_3 = 16{\cdot}5$ mm, $r_4 = 47{\cdot}5$ mm, $h_1 = 2{\cdot}0$ mm, $h_2 = 2{\cdot}4$ mm, $h_3 = 6{\cdot}0$ mm, $h = 9{\cdot}6$ mm, $S = 15{\cdot}0$ mm, $b_1 = 4{\cdot}0$ mm, $b_2 = 12{\cdot}9$, and $h_D = 0{\cdot}8$ mm. On the other hand, the relevant material properties are such that $E_S = E_D = 7{\cdot}2 \times 10^{10}$ N/m^2, $v = 0{\cdot}3$, $\rho_S = \rho_D = 2750$ kg/m^3, $k_B = 3{\cdot}0 \times 10^{10}$ N/m, and $c_B = 100$ Ns/m. However, any damping inherent in the system including c_B is to be neglected in computations. Besides, the inner radius of the disk, r_3, is in fact set at 15 mm, instead of 16·5 mm, because the effective inner radius tends to be smaller than the spacer's outer radius when disks are sufficiently and literally clamped.

Its modal characteristics are studied with the shaft element meshes increased up to 13 for the hub part including the spindle, the spacers in between disks, and the clamp atop as the geometry dictates. As a result, the coupled vibrational modes take the natural frequencies and the mode shapes as in Figures 9 and 10, respectively, whereas the uncoupled disk modes are computed as in Figure 11. Just as with the first and the third coupled modes of the preceding two-disked example, the first and the fourth coupled modes here are 180° out of phase in view of the disk's deflections relative to the spindle. Such modes are the typical ones which cannot be discriminated in case the spindle or the disks are individually analyzed.

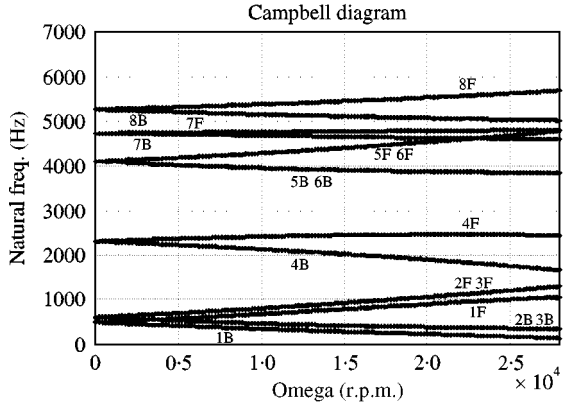

Figure 9. Coupled modes (3 disks).

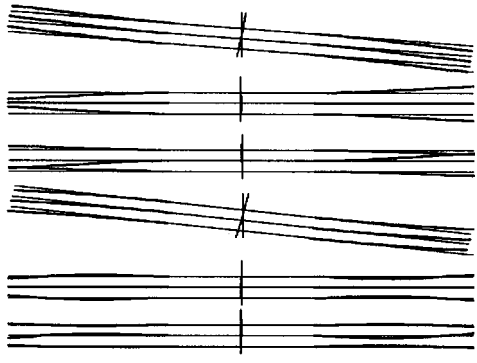

Figure 10. Mode shapes (3 disks): from the top, first to sixth mode.

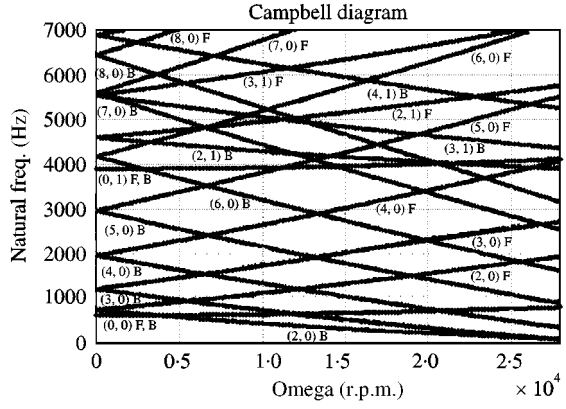

Figure 11. Uncoupled disk modes (3 disks).

Comparisons between Figures 7 and 9 allow one to predict that in the same frequency range, more coupled modes will appear as the number of stacked disks increases, raising the chances of resonance at a specific rotational speed.

In principle, the uncoupled disk modal characteristics should be identical as long as the hard disks are of the same specifications. However, the natural frequencies in Figure 11 are

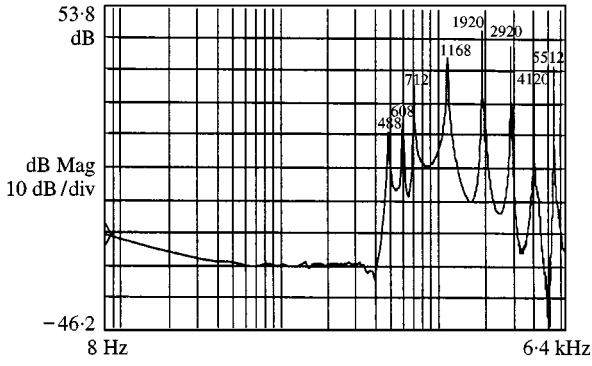

Figure 12. FRF at 0 rpm (3 disks).

generally lower than those in Figure 8. This is because the inner radius of the disk is tuned to be 15 mm in the computation for three-disked HDD other than 17 mm, the value used in the case of the two-disked HDD merely to be consistent with reference [5] where the concept of effective inner radius is overlooked.

4.3. FREQUENCY RESPONSES

Finally, the frequency response functions (FRFs) are experimentally found as well by the impact test to confirm the natural frequencies and identify the magnitudes of the concerned modes in the HDD sample with triple disks. The experiments are performed with the HDD cover screwed on the fixed shaft as in normal usage.

When the spindle is stationary, the FRF in Figure 12 is obtained by striking the top disk near the rim with a pencil-type impulse hammer and measuring output velocity signal via a laser doppler vibrometer pointed at the vicinity. The figure shows peaks of the lowest two coupled disk modes and seven uncoupled disk modes such as $(0,0)$, $(2,0)$–$(7,0)$ in the increasing order of nodal diameters with no nodal circles. Compared to such a wide frequency range, the second coupled mode is so closely spaced with the $(0,0)$ mode as to be hardly discernible from it. Furthermore, it is self-evident that the higher modes missing within the frequency range of Figure 12 are difficult to detect due to their small magnitudes. Table 1 shows that the mean error is about 1·5% between the actual peak frequencies and the computed ones enlisted from values in Figures 9 and 11.

On the other hand, the FRF during rotation at a speed of 7200 rpm is obtained as in Figure 13 in the same fashion. Aside from the peaks including the first two, most modes in Figure 12 consistently appear. As predicted, the forward and backward whirls split in the modes subject to the gyro effects. In Table 2, the experimental natural frequencies are found to deviate about 1·9% from the computed ones on average.

It is also remarkable that at the integer multiple frequencies of the rotational speed such as 120 and 240 Hz, extra peaks are observed resulting from the disk surface waviness or the assembly tolerance in the HDD system. In order to indicate the mobility magnitude at each mode, the ordinate readings of Figures 12 and 13 are marked in the decibel values of mm/Ns.

As the principal source of errors between the computational and the experimental results, ignorance of the following factors can be pointed out in the case of coupled modes; longitudinal and axial vibrations, the small protruding hub portion in contact with the

TABLE 1

Natural frequencies at 0 *rpm*

No.	Mode shape	Comp. (Hz)	Exp. (Hz)	Error (%)
1	1st coupled	489	488	0·2
2	2nd coupled	602	608	0·98
3	(0,0)	615	608	1·15
4	(2,0)	731	712	1·1
5	(3,0)	1188	1168	1·6
6	(4,0)	1955	1920	2·0
7	(5,0)	2963	2920	1.4
8	(6,0)	4182	4120	1·5
9	(7,0)	5598	5512	1·5

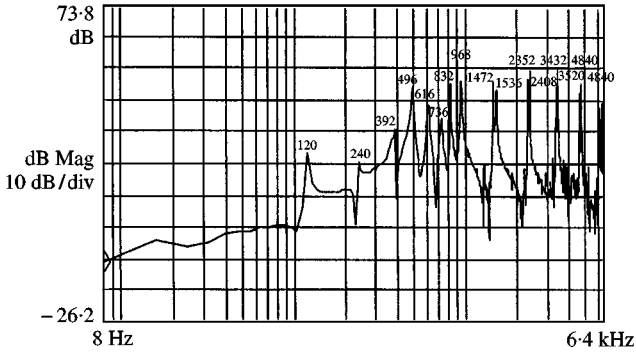

Figure 13. FRF at 7200 rpm (3 disks).

TABLE 2

Natural frequencies at 7200 *rpm*

No.	Mode shape	Comp. (Hz)	Exp. (Hz)	Error (%)
1	1st coupled, B	385	392	1·78
2	(2,0) B	518	496	4·2
3	1st coupled, F	621	616	0·8
4	(3,0) B	857	832	2·9
5	(2,0) F	989	968	2·1
6	(4,0) B	1503	1472	2·0
7	(3,0) F	1563	1536	1·7
8	(5,0) B	2392	2352	1·6
9	(4,0) F	2455	2408	1·9
10	(6,0) B	3491	3432	1·7
11	(5,0) F	3570	3520	1·4
12	(6,0) F	4905	4840	1·3

lower bearing, and its associated bearing location discrepancy. On the other hand, in the case of uncoupled disk modes, primary errors depend on how accurate the disk's effective inner radius dimension is. Moreover, it should be noted that in the computations of both coupled and uncoupled modes, any damping is neglected. Therefore, it is unavoidable that

the natural frequencies are evaluated to be slightly higher than they are even if the mode shapes having nothing to do with it.

5. CONCLUSIONS

Finite element models for HDD spindle systems were formulated taking into account the structural flexibility of every component and the centrifugal effect particularly on disks. By means of them, their coupled flexural vibrations as well as the uncoupled ones could be computed up to fairly high modes using only a few element meshes. Those results were confirmed to be effective and accurate enough by experiments.

It is also observed that the more disks are stacked in a HDD system, the more coupled vibrational modes appear within the given low-frequency range even if the uncoupled disk nodes remain unaltered. This implies more chances of resonance in proportion. The proposed approach may significantly enhance the design capability for the high-speed and high density HDDs and the likes to come.

ACKNOWLEDGMENTS

The author wishes to thank Dr. S. B. Chun for his comments on this work and also my graduate students, B. M. Kwak and I. J. Jae for preparation of this manuscript.

REFERENCES

1. C. W. Lee, S. W. Park and K. H. Rim 1989 *Proceedings of ASIA Vibration Conference*, 439–444. Free vibration of a spinning annular disk subjected to radial tension.
2. A. A. S. Shahab and J. Thomas 1987 *Journal of Sound and Vibration* **114**, 435–452. Coupling effects of disc flexibility on the dynamic behavior of multi disc-shaft systems.
3. I. Y. Shen and C. P. R. Ku 1997 *Journal of Applied Mechanics* **64**, 165–169. A nonclassical vibration analysis of a multiple rotating disk and spindle assembly.
4. G. Genta and A. Tonoli 1996 *Journal of Sound and Vibration* **196**, 19–43. A harmonic finite element for the analysis of flexural, torsional and axial rotordynamic behavior of discs.
5. C. W. Lee and S. B. Chun 1998 *Journal of Vibration and Acoustics* **120**, 87–94, Vibration analysis of a rotor with multiple flexible disks using the assumed modes method.
6. H. S. Jia, S. B. Chun and C. W. Lee 1997 *Journal of Sound and Vibration* **208**, 175–187. Evaluation of the longitudinal coupled vibrations in rotating, flexible disks/spindle systems.
7. C. W. Lee, H. S. Jia, C. S. Kim and S. B. Chun 1997 *Journal of Sound and Vibration* **207**, 435–451. Tuning of simulated natural frequencies for a flexible shaft-multiple flexible disk system.
8. L. Meirovitch 1967 *Analytical Methods in Vibrations*. London: Macmillan Company.
9. A. C. Ugural and S. K. Fenster 1981 *Advanced Strength and Applied Elasticity*. New York: Elsevier.
10. J. N. Reddy, 1985 *An Introduction to the Finite Element Method*. New York: McGraw-Hill.

APPENDIX A: KINETIC ENERGY OF THE ANNULAR DISK ELEMENT

$$T_D^e = \tfrac{1}{2}\Omega^2 \mathbf{q}_y^{\mathrm{T}} \{m_D^e \Psi_S(x_D) + (I_{Dy} - I_{Dp})\Phi_S(x_D)\}\mathbf{q}_y + \tfrac{1}{2}\Omega^2 q_z^{\mathrm{T}} \{m_D^e \Psi_S(x_D) + (I_{Dy} - \mathrm{I}_{Dp})\Phi_S(x_D)\}\mathbf{q}_z$$

$$+ \tfrac{1}{2}\dot{\mathbf{q}}_y^{\mathrm{T}} \{m_D^e \Psi_S(x_D) + I_{Dy}\Phi_S(x_D)\}\dot{\mathbf{q}}_y + \tfrac{1}{2}\dot{\mathbf{q}}_z^{\mathrm{T}} \{m_D^e \Psi_S(x_D) + I_{Dy}\Phi_S(x_D)\}\dot{\mathbf{q}}_z$$

$$+ \Omega \mathbf{q}_y^{\mathrm{T}} \{m_D^e \Psi_S(x_D) + (I_{Dy} - I_{Dp})\Phi_S(x_D)\}\dot{\mathbf{q}}_z - \Omega \mathbf{q}_z^{\mathrm{T}} \{m_D^e \Psi_S(x_D) + I_{Dy}\Phi_S(x_D)\}\dot{\mathbf{q}}_y$$

$$+ \Omega(\dot{\mathbf{q}}_y^{\mathrm{T}}\Phi_{SD}(x_D)\mathbf{q}_{Dc} - \dot{\mathbf{q}}_y^{\mathrm{T}}\Phi_{SD}(x_D)\mathbf{q}_{Ds} + \mathbf{q}_z^{\mathrm{T}}\Phi_{SD}(x_D)\dot{\mathbf{q}}_{Dc} - \mathbf{q}_y^{\mathrm{T}}\Phi_{SD}(x_D)\dot{\mathbf{q}}_{Ds}\}$$

$$+ \Omega^2\{\mathbf{q}_y^{\mathrm{T}}\Phi_{SD}(x_D)\mathbf{q}_{Dc} + \mathbf{q}_z^{\mathrm{T}}\Phi_{SD}(x_D)\mathbf{q}_{Ds}\} - \dot{\mathbf{q}}_y^{\mathrm{T}}\Phi_{SD}(x_D)\dot{\mathbf{q}}_{Dc} - \dot{\mathbf{q}}_z^{\mathrm{T}}\Phi_{SD}(x_D)\dot{\mathbf{q}}_{Ds}$$

$$+ \tfrac{1}{2}\{I_{Dp}\Omega^2 + \dot{\mathbf{q}}_{Dc}^{\mathrm{T}}M_D^e\dot{\mathbf{q}}_{Dc} + \dot{\mathbf{q}}_{Ds}^{\mathrm{T}}M_D^e\dot{\mathbf{q}}_{Ds}\}.$$

APPENDIX B: STIFFNESS MATRICES OF THE ANNULAR DISK ELEMENT

$$K_{De} = \int_{R_i}^{R_0} \pi D_E[\boldsymbol{\varphi}_D''\boldsymbol{\varphi}_D''^{\mathrm{T}} - \frac{v}{r}\boldsymbol{\varphi}_D''\left(\boldsymbol{\varphi}_D'^{\mathrm{T}} - \frac{\boldsymbol{\varphi}_D^{\mathrm{T}}}{r}\right) - \frac{v}{r}\left(\boldsymbol{\varphi}_D' - \frac{\boldsymbol{\varphi}_D}{r}\right)\boldsymbol{\varphi}_D''^{\mathrm{T}}$$

$$+ \frac{(3-2v)}{r^2}\left(\boldsymbol{\varphi}_D' - \frac{\boldsymbol{\varphi}_D}{r}\right)\left(\boldsymbol{\varphi}_D'^{\mathrm{T}} - \frac{\boldsymbol{\varphi}_D^{\mathrm{T}}}{r}\right)\Bigg] r\,\mathrm{d}r,$$

$$D_E = E_D h_D^3/12(1-v^2),$$

$$K_{De} = \int_{R_i}^{R_0} \pi h_D[\sigma_r\boldsymbol{\varphi}_D'\boldsymbol{\varphi}_D'^{\mathrm{T}} + \sigma_\theta\boldsymbol{\varphi}_D\boldsymbol{\varphi}_D^{\mathrm{T}}/r^2]r\,\mathrm{d}r.$$